PAPER

Tailoring the photo-Fenton activity of spinel ferrites (MFe$_2$O$_4$) by incorporating different cations (M = Cu, Zn, Ni and Co) in the structure†

Rimi Sharma,[a] S. Bansal[b] and Sonal Singhal*[a]

Magnetic bimetallic nanospinels (MFe$_2$O$_4$; M = Cu, Zn, Ni and Co) with sizes ranging between 15–30 nm were synthesized using a facile and viable sol–gel method. Fourier transform infrared spectral analysis of all the samples demonstrated the formation of M–O bond in the spinel structure. Structural exploration of all the nano materials using powder X-ray diffraction and high resolution transmission electron microscopy revealed the formation of a single phase cubic spinel structure. All the materials exhibited a magnetic temperament with high surface areas (92–151 m^2 g^{-1}). Furthermore, the band gaps calculated from the diffuse reflectance spectra were quite narrow (1.26–2.08 eV) for all the samples, hence the ferrites could act as visible light driven photocatalysts. The prepared nanospinels are proposed to be promising heterogeneous photo-Fenton catalysts under visible light for the degradation of organic pollutants. The catalytic results revealed that the rate of reaction was significantly influenced by the cation in the spinel structure as the degradation order was observed to be CuFe$_2$O$_4$ (k = 0.286 min^{-1}) > ZnFe$_2$O$_4$ (k = 0.267 min^{-1}) > NiFe$_2$O$_4$ (k = 0.138 min^{-1}) > CoFe$_2$O$_4$ (k = 0.078 min^{-1}). The reaction conditions were optimized for all the ferrites as the photodegradation was influenced by the ferrite dosage (0.25–1.00 g L^{-1}), pH (2–5) and the H$_2$O$_2$ concentration (4–27 mM). The experimental data disclosed that the ferrite activity was sensitive to sintering temperature. The materials displayed remarkable stability in the reaction as they could be magnetically separated using an external magnet and recycled for up to 4 consecutive cycles. There was no significant loss in activity of all the materials, demonstrating the excellent ability of the ferrites to remove organic pollutants from wastewater.

1. Introduction

In the present scientific world, development of environmentally benign catalysts is of significant importance. The most vital feature of a green catalyst for industrial application is the capability to be efficiently recovered after the reaction.[1] Conventional catalyst isolation methods, such as chromatography, filtration, and centrifugation, are monotonous and cause a lot of inconvenience.[2] To overcome these issues, the concept of magnetically separable nanocatalysts is emerging as a robust and highly efficient alternative. The inherent magnetic characteristic of these materials allows simple and efficient separation from the reaction mixture, thereby minimizing the required work up procedures.[3] Consequently, the sustainability of magnetic catalysts satisfies the principles of green chemistry.

In the magnetic nanomaterials class, magnetite (Fe$_3$O$_4$) is one of the simplest ferrospinels[4] that has attracted considerable attention and is being intensely investigated in different reactions. The properties of magnetite are engineered by introduction of cations, such as Co, Ni, Cu, Mn, and Zn, into its structure. These modified ferrospinels, commonly known as ferrites, have the general formula MFe$_2$O$_4$ (M = Co, Ni, Cu, Zn, Mn). In ferrites, substitution of iron with a second metal improves the properties as well as the catalytic scope while the iron component enables magnetic recovery of the catalyst after the reaction.[5] Spinel ferrites are emerging as the focus of recent scientific research due to their excellent catalytic performance in reactions such as CO$_2$ reduction,[6] coupling reactions,[7] methane oxidative conversion,[8] and water gas shift reaction,[9] and as an adsorbent for the removal of toxic substances.[10]

These materials have an important characteristic of a narrow band gap, which lies in the visible region.[11] This property allows ferrites to efficiently utilize the visible region of the solar spectrum in photocatalytic reactions such as the oxidative dehydrogenation of hydrocarbons,[12] decomposition of H$_2$O$_2$,[13] and the degradation of different organic pollutants.[14–16] In addition to these applications, ferrites can be used as potential photo-Fenton catalysts as they enhance the oxidizing power of Fenton type reactions. Hitherto, many authors have focused their research on the degradation of organic pollutants in aqueous

^{a}*Department of Chemistry, Panjab University, Chandigarh, 160014, India. E-mail: sonal1174@gmail.com*

^{b}*DST, New Delhi, India*

solutions using ferrites. For instance, researchers have illustrated the role of zinc ferrite ($ZnFe_2O_4$) nanoparticles in the photodegradation of different dyes under visible light.[17,18] Mahmoodi observed low performance for the photodegradation of Reactive Red 198 (RR198) and Reactive Red 120 (RR120) in the absence of ferrite.[17] Mesoporous $ZnFe_2O_4$ was employed by Su et al. for photocatalytic degradation of Acid Orange II (AOII) dye under visible light/H_2O_2 system.[18] Similarly monodisperse cobalt ferrite ($CoFe_2O_4$) nanoparticles of 2–6 nm size were employed by Feng et al. for the degradation of methylene blue dye.[19] The use of bismuth ferrite ($BiFeO_3$) for photodegradation reactions has been explored by different researchers.[20–22]

To the best of our knowledge, no research has been carried out on modulating the photo-Fenton activity by altering the cation within the ferrite. In this context, herein we report a simple and facile fabrication of spinel ferrites (MFe_2O_4; M = Cu, Zn, Ni and Co) using sol–gel methodology. The prepared materials were characterized using diverse techniques. The application of these materials was demonstrated in a heterogeneous photo-Fenton degradation reaction. In the present study, methylene blue (MB) dye was used as a model pollutant. The properties of ferrites strongly depend on the cation present in the spinel structure; hence, the present aim is to study the comparative effects of different ferrites on the degradation reaction. The influence of various parameters such as catalyst loading, dye concentration, initial pH of dye solution, annealing temperature and H_2O_2 concentration on the degradation reaction in the presence of all the ferrites was studied. Furthermore, verification of the main active species responsible for degradation, i.e. the hydroxyl radical ($^•OH$), was also carried out. Finally, the recyclability of the catalyst was evaluated for 4 consecutive cycles without any significant loss in activity, indicating the good stability of the material.

2. Experimental section

2.1 Materials

Ferric nitrate ($Fe(NO_3)_3 \cdot 9H_2O$, 98%), cupric nitrate ($Cu(NO_3)_2 \cdot 3H_2O$, 99.5%), nickel nitrate ($Ni(NO_3)_2 \cdot 6H_2O$, 98%), zinc nitrate ($Zn(NO_3)_2 \cdot 6H_2O$, 96%), cobalt nitrate ($Co(NO_3)_2 \cdot 6H_2O$, 99%), citric acid (99.57%) and hydrogen peroxide (30% w/v) were procured from Fisher Scientific. Ethylene glycol (99%) and methylene blue were supplied by Merck and CDH, respectively. All the chemicals were of analytical grade, commercially available and used without further purification.

2.2 Synthesis of ferrite

Ferrites with the general formula MFe_2O_4 (M = Co, Ni, Zn, Cu) were synthesized using a modified version of a previously reported sol–gel method.[23,24] In a typical procedure to synthesize $ZnFe_2O_4$, stoichiometric amounts of zinc nitrate (0.02 moles, 5.949 g) and ferric nitrate (0.04 moles, 16.16 g) were dissolved in a minimum amount of distilled water with magnetic stirring at 80–90 °C. After complete dissolution, citric acid (in the molar ratio 1 : 1 to precursor metal salts) and ethylene glycol (10 mL)

were added into the above solution and stirred until gel formation. The gels were dried and crushed to obtain a ferrite powder. Finally, annealing was carried out at 400 °C and 1000 °C for 2 hours in muffle furnace before further characterization and application. A similar procedure was followed for the synthesis of the other ferrites.

2.3 Photocatalytic activity

The photocatalytic performance of prepared ferrites was evaluated by degradation of MB in aqueous solution. All the experiments were performed at room temperature under ambient conditions. For the degradation reactions, a stock solution of 10 mg L^{-1} MB was prepared in distilled water. In all the experiments, the molar ratio of H_2O_2/MB/ferrite was fixed at 1/0.001/0.065. In a typical reaction, the desired amount (25–100 mg) of ferrite nanoparticles was dispersed in 100 mL of MB solution (pH 2.5 using H_2SO_4). Prior to irradiation under an Xe lamp, the suspension was magnetically stirred in the dark for 30 minutes, followed by addition of H_2O_2. 3 mL aliquots of dye solution were taken out at regular time intervals and the catalyst was separated. The change in concentration of the degraded solution was analyzed using UV-vis spectroscopy. The photodegradation study was performed by varying different reaction conditions, such as catalyst loading, dye concentration, pH, H_2O_2 dosage and annealing temperature, under similar reaction conditions.

2.4 Physical characterization

Thermogravimetric analysis was performed by heating the raw samples on a thermal analyzer (SDT Q600) at a heating rate of 10 °C min^{-1}. The presence of an M–O bond in the ferrites was detected using a Fourier transform infrared spectrophotometer (PerkinElmer) in the range 800–400 cm^{-1}. A high resolution transmission electron microscope (FEI Tecnai, G2 F20) with an accelerating voltage of 200 keV was used to calculate the particle size of the photocatalysts. The phase purity and structural properties of the samples were investigated using an X-ray diffractometer (model Bruker AXS, D8 Advance) with radiation from a Cu target (Cu K_α = 1.54 Å). Optical properties were probed by diffuse reflectance spectroscopy by means of a UV-vis absorption spectrophotometer (Analytikjena Specord 205). Magnetic characterization as a function of magnetic field (± 10 kOe) was scrutinized at room temperature using a vibrating sample magnetometer (155, PAR). A Brunauer–Emmett–Teller (BET) surface area analyzer (11-2370, Gemini, Micromeritics, USA) was used to measure the surface area. A 150 W Xe lamp with 96 000 Lux was used as the visible light source. The concentration of MB was analyzed using a UV-vis spectrophotometer (JASCO, V-530).

3. Characterization of catalysts

3.1 Thermogravimetric analysis (TGA)

The combustion process of all the as prepared ferrite samples was investigated using TGA. The typical TGA curves of the as obtained $NiFe_2O_4$ shown in Fig. SF1 (ESI†) exhibited

decomposition in two weight loss steps. The first stage was observed at around 50–100 °C owing to the loss of water molecules from the sample. The second weight loss in the range of 300–400 °C was ascribed to the decomposition of ethylene glycol and nitrates into CO_2 and NO_x, respectively.[25,26] When the temperature was increased beyond 400 °C, no further weight loss was observed, indicating the formation of pure $NiFe_2O_4$. Similar TGA curves were obtained for the other ferrite samples. Therefore, all the ferrite samples were sintered at a minimum temperature of 400 °C before characterization.

3.2 Fourier transform infrared (FTIR) spectroscopy

The peaks in the FTIR spectra are due to the vibration of ions in the crystal lattice. The presence of a metal–oxygen (M–O) bond in the ferrites was supported by this study. The room temperature FTIR spectra of all the ferrites annealed at 400 °C and 1000 °C are shown in Fig. SF2 (A) and (B), respectively (ESI†). Both the graphs depict two vibration bands in the range of 600–400 cm^{-1} for all the ferrites. The band at higher frequency (ν_{tet}) was assigned to the stretching vibration between the tetrahedral metal ions and the oxygen ion (M_{tet}–O), while the band at lower frequency (ν_{oct}) was attributed to the stretching vibration of bonds between the octahedral metal ions and the oxygen ion (M_{oct}–O).[27]

3.3 High resolution transmission electron microscopy (HRTEM)

HRTEM was used to examine the size, distribution and crystallinity of particles in all the ferrites. The synthesized sample was dispersed in absolute ethanol and a few drops of the dispersion were placed on a carbon grid in order to obtain HRTEM images. A typical low resolution TEM micrograph of $CuFe_2O_4$ obtained after annealing at 400 °C is shown in Fig. 1(a). The results indicate that the particles were highly agglomerated due to the magnetic characteristic of ferrites.[28] The average particle size was around 15 nm, which was consonant with the XRD results. In a similar manner, the particle sizes of other ferrites were obtained and are listed in Table ST1 (ESI†).

The particle size of the samples crucially depends on the temperature of the heat treatment. An increase in particle size was observed in samples annealed at higher temperatures due to fusion of neighboring particles. The TEM image of $CuFe_2O_4$ annealed at 1000 °C is given in Fig. 1(b). The image indicates the enhancement in the particle size with the increase in annealing temperature from 400 °C to 1000 °C. Such an increase in particle size with annealing temperature is consistent with earlier reports.[29]

HRTEM study revealed that all the nanoparticles were crystallized into single ferrite crystals. The HRTEM images of the $CuFe_2O_4$ nanoparticles at magnifications of 2 nm and 5 nm are shown in Fig. 1(c) and (d), respectively. The crystallite planes were judged from the measured average fringe width values labeled on the HRTEM image. The average fringe width calculated from the profile of the frame (Fig. 1(e)) was observed to be 0.25 nm corresponding to the (311) plane, which was the most

intense peak obtained in XRD. The live FFT of $CuFe_2O_4$ is given in the inset of Fig. 1(c) and the reconstructed image after filtering the FFT pattern from HRTEM is given in Fig. 1(f).

3.4 Powder X-ray diffraction (XRD) studies

The crystal structure, phase purity and crystallite size of the synthesized nano ferrites were investigated using powder XRD. The XRD patterns of all the ferrites annealed at 400 °C and 1000 °C are shown in Fig. 2. For all the ferrites annealed at 400 °C, diffraction peaks corresponding to the (hkl) (220), (311), (400), (511) and (440) planes can be readily indexed to the formation of a single phase cubic spinel structure according to JCPDS card no. 01-089-1012, 00-001-1121, 01-077-0010 and 00-003-0875 for $ZnFe_2O_4$, $CoFe_2O_4$, $CuFe_2O_4$ and $NiFe_2O_4$, respectively. A close examination of XRD patterns illustrated that the peak intensity gradually increased and became narrow with an increase in the annealing temperature from 400 °C to 1000 °C. Thus, the samples became crystalline with annealing. All the ferrites were stable to heat treatment as the cubic spinel structure was retained in the case of $ZnFe_2O_4$, $CoFe_2O_4$ and $NiFe_2O_4$. However, in the case of $CuFe_2O_4$ the spinel structure was transformed into tetragonal. This transformation of the structure of $CuFe_2O_4$ has been reported in the literature.[30]

The crystallite size was calculated using the most intense peak broadening of the 311 plane with the help of the Debye–Scherrer formula.[31] The crystallite sizes for the samples annealed at 400 °C varied between 15–30 nm and are given in Table ST1 (ESI†). Lattice parameter for all the ferrites annealed at 400 °C were calculated using the Le Bail refinement method and were in the range of 8.35–8.44 Å, which is consistent with the earlier reported values (Table ST1, ESI†).[32–34]

3.5 Optical properties

Optical properties are a key factor in designing highly efficient photocatalysts. The typical UV-vis diffuse reflectance spectrum of $ZnFe_2O_4$ presented in Fig. 3(a) demonstrates an absorption edge around 730 nm, illustrating its suitability for visible light photocatalysis. The ferrites could absorb a considerable amount of visible light due to electron excitation from the O-2p level (valence band) to the Fe-3d level (conduction band).[35] The optical band gap was estimated using the following equation:[15]

$$\alpha h\nu = A(h\nu - E_g)^{n/2} \qquad (1)$$

where α is the absorption coefficient, ν is the light frequency, E_g is the band gap, h is Planck's constant and A is a constant. The band gap calculated from the plot of $(\alpha h\nu)^2$ versus $h\nu$ (photon energy) was 1.94 eV (Fig. 3(b)), which is in close agreement with the value reported in the literature.[11] Similarly, the band gaps of the other materials were calculated and the values varied between 1.26–2.08 eV (Table ST1, ESI†). The band gaps were quite narrow, hence all the ferrites could act as visible light driven photocatalysts.
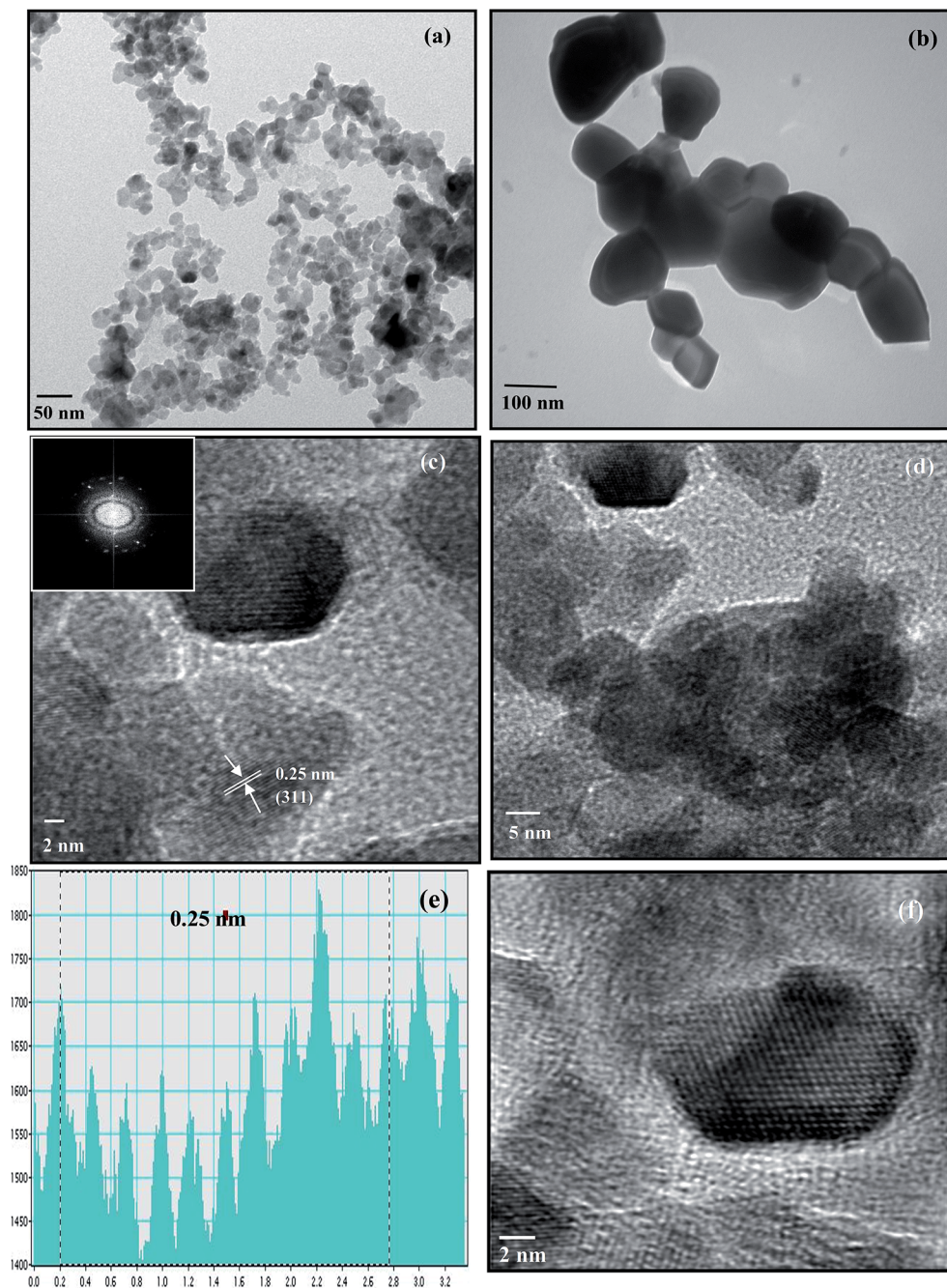
Fig. 1 TEM images of CuFe$_2$O$_4$ annealed at (a) 400 °C and (b) 1000 °C, HRTEM images of the CuFe$_2$O$_4$ nanoparticles at (c) magnification of 2 nm (inset shows the FFT of CuFe$_2$O$_4$) and (d) magnification of 5 nm. (e) Frame profile for the average fringe width. (f) Reconstructed image after filtering the FFT pattern from HRTEM.

3.6 Magnetic study

The magnetic characteristic of a material is a crucial property which is determined by recording magnetization curves at room temperature using a vibrating sample magnetometer (VSM). The hysteresis loop of all the samples annealed at 400 °C shown in Fig. 4 clearly illustrates their magnetic behavior. Different parameters such as saturation magnetization (M_s) and coercivity (H_c) deduced from the magnetization curves are listed in Table ST1 (ESI†). From Fig. 4 and the values listed

in Table ST1,† it is clear that the coercivity of CoFe$_2$O$_4$ is very high as compared to the other samples, which is a typical behavior of hard ferrites. Therefore, it can be concluded that CoFe$_2$O$_4$ is a hard ferrite while the rest of the samples are soft ferrites.

Furthermore, the M_s of CoFe$_2$O$_4$ and CuFe$_2$O$_4$ is much higher than other two samples (M_s is 6, 19, 60 and 65 emu g^{-1} for ZnFe$_2$O$_4$, NiFe$_2$O$_4$, CuFe$_2$O$_4$ and CoFe$_2$O$_4$, respectively). In addition, it was observed that saturation magnetization at the
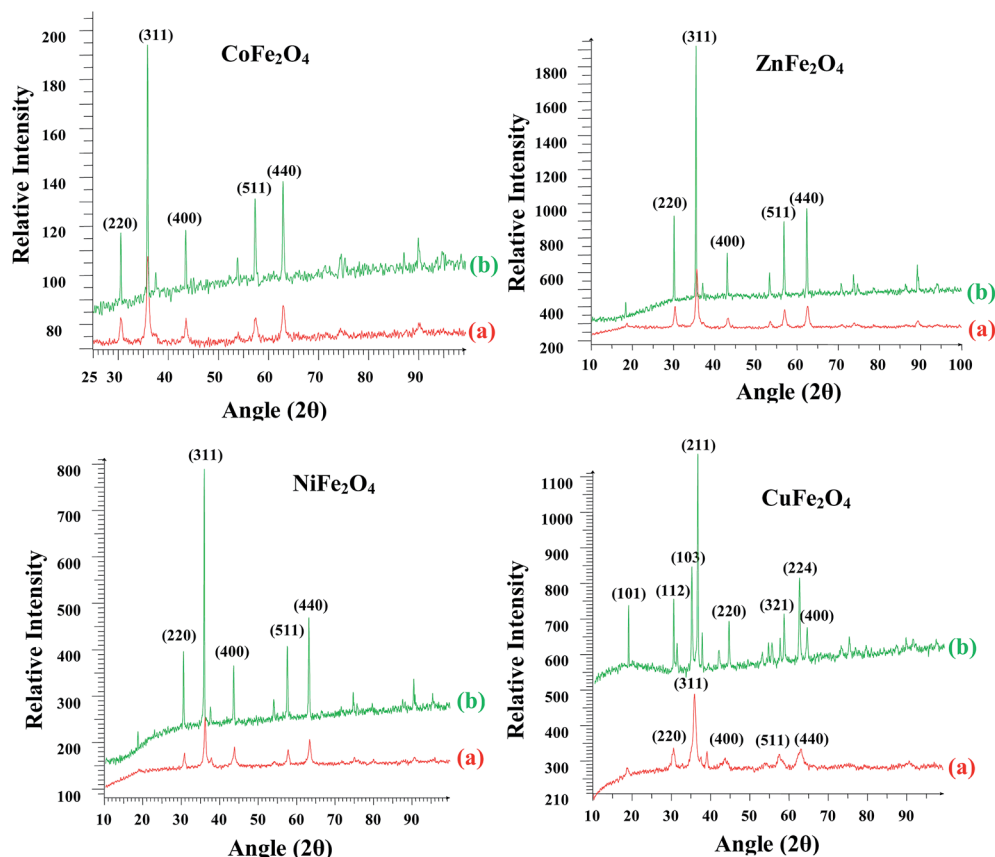
Fig. 2 Powder X-ray diffractograms of the ferrites annealed at (a) 400 °C and (b) 1000 °C.

nano range is lower as compared to its bulk counterpart which may be due to the small size, surface disorder and modified cation distribution at the nano level.[36] From this study, it is concluded that all the ferrites can be magnetically separated from the reaction mixture using an external magnet for many cycles without any significant loss.

3.7 BET surface area analysis

The surface area of all the synthesized spinel ferrites was estimated using a Brunauer–Emmett–Teller (BET) surface analyzer at −196 °C. The sample was prepared at 150 °C for 2 hours with the flow of N_2 gas. The concept of BET is an extension of Langmuir theory and is based on the BET equation proposed by Brunauer, Emmett and Teller.[37]

$$\frac{1}{Q\left[\left(\frac{P_0}{P}\right) - 1\right]} = \frac{C-1}{Q_m C}\left(\frac{P}{P_0}\right) + \frac{1}{Q_m C} \tag{2}$$

where P is the equilibrium pressure, P_0 is the saturation pressure, Q is the quantity of the gas adsorbed on the adsorbate, Q_m is the monolayer adsorbed gas quantity and C is the BET
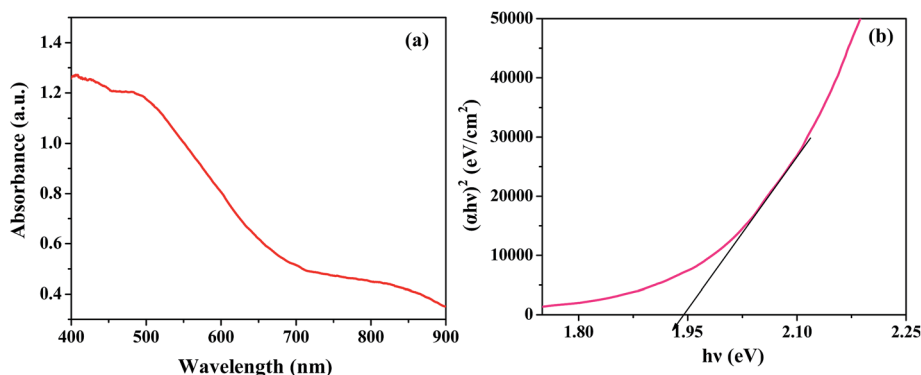

Fig. 3 (a) Diffuse reflectance spectra and (b) $(\alpha h\nu)^2$ vs. $h\nu$ plot of $ZnFe_2O_4$ annealed at 400 °C.
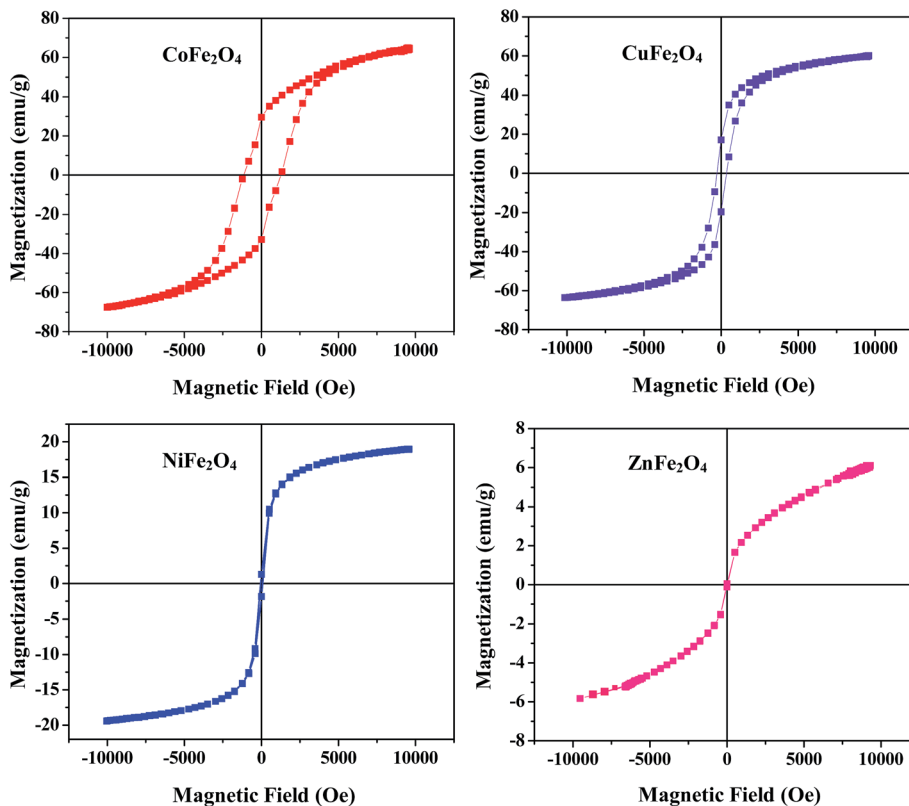
Fig. 4 Magnetic hysteresis loops for the ferrites annealed at 400 °C.

constant. The BET plots ($1/[Q(P_0/P)]$ *vs.* P/P_0) of all the samples are given in Fig. 5. The plots were observed to be linear and unique values of Q_m and C were estimated from the slopes (A)

and intercepts (I) according to the equations given in the ESI.† Different variables calculated from the BET plots such as slope, intercept, Q_m, C, S_{total} and S_{BET} are listed in Table 1. The BET
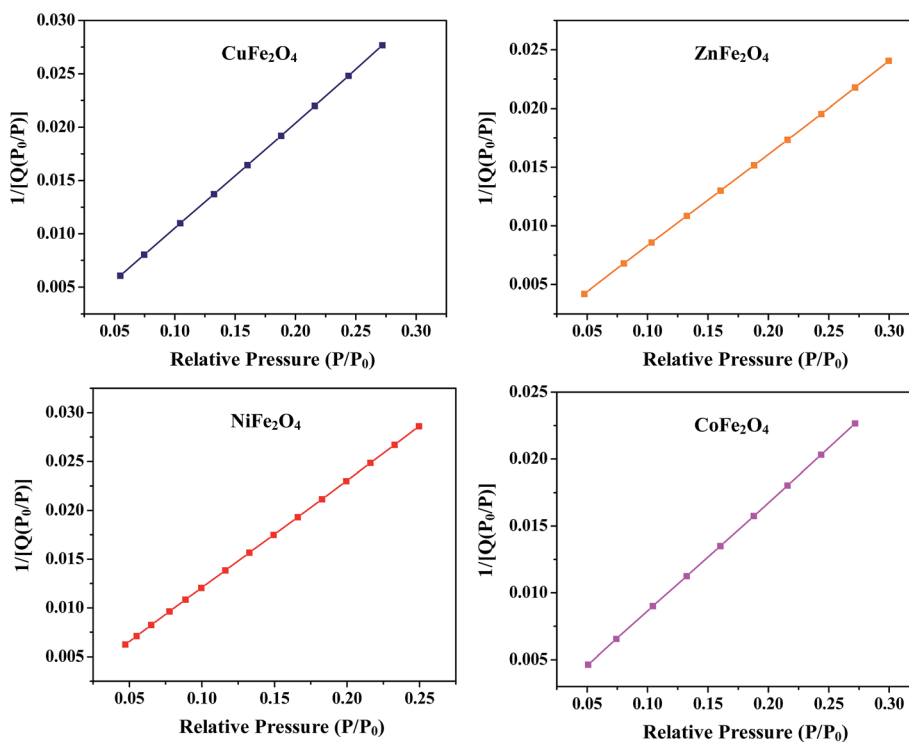

Fig. 5 BET plots of the ferrites annealed at 400 °C.

Table 1 Parameters calculated from the BET plots of the ferrites annealed at 400 °C

Ferrite	Slope (g cm^{-3})	Intercept (g cm^{-3})	Q_m (cm^3 g^{-1})	C	S_{total} (m^2 g^{-1})	S_{BET} (m^2 g^{-1})
$CuFe_2O_4$	0.099205	0.000599	10.0196	166.600191	~43	~97
$ZnFe_2O_4$	0.078485	0.000446	12.6693	176.966319	~55	~151
$NiFe_2O_4$	0.11805	0.001056	8.9976	105.259751	~40	~92
$CoFe_2O_4$	0.081386	0.000481	12.2149	170.076638	~53	~137

surface areas of all the synthesized samples were found to be in the range of 92–151 m^2 g^{-1}.

4.   Photocatalytic activity

Photo-Fenton activity was investigated by measuring the rate of degradation of the aqueous MB solution in the presence of the ferrites under visible light irradiation. The UV-vis spectrum of MB contained 4 absorption peaks at 664 nm, 617 nm, 292 nm and 246 nm. The essential peak at 664 nm was in the visible region with a shoulder at 617 nm and the other two peaks were in the UV region. The major band at 664 nm appeared due to conjugation between two dimethylamine substituted aromatic rings through S and N and the peaks in the ultraviolet region were assigned to the aromatic rings.[38,39]

4.1   Control experiment

Various control experiments were designed for the degradation of MB in the presence of all the ferrites. The typical results for $NiFe_2O_4$ are illustrated in Fig. 6(A). Under visible light irradiation MB exhibited ~10% decomposition (Fig. 6(A)(a)) while no significant degradation of MB was observed in the absence of a ferrite (MB + H_2O_2 only) both in the dark and in the presence of light (Fig. 6(A)(b and c)). Experiments were also carried out in the absence of H_2O_2 (MB + ferrite only) in both dark and light conditions. The results showed no appreciable degradation with time (Fig. 6(A)(d and e)). In the absence of light (MB + H_2O_2 + ferrite), although ~30% degradation was observed (Fig. 6(A)(f)), the degradation was greatly enhanced to ~99% in
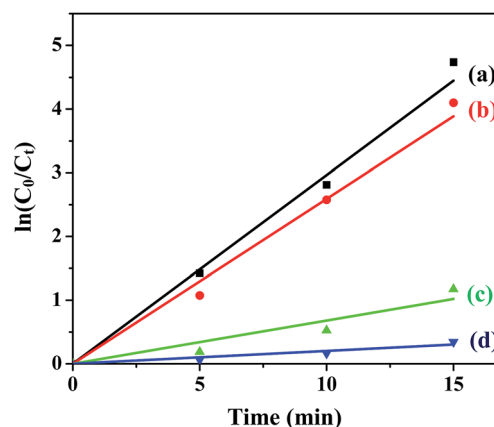
Fig. 7 Photodegradation kinetics of MB in the presence of (a) $CuFe_2O_4$, (b) $ZnFe_2O_4$, (c) $NiFe_2O_4$ and (d) $CoFe_2O_4$ under optimum conditions.

Table 2 Variation of rate constants with catalyst loading in the presence of ferrites

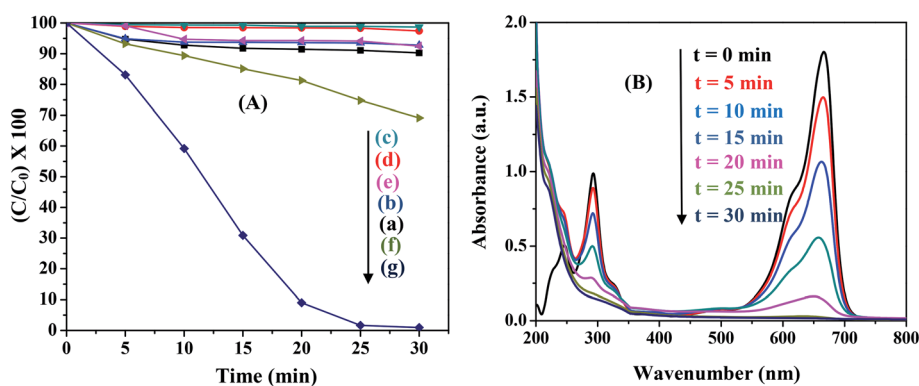| Ferrite	Catalyst loading (g L^{-1})			
	0.25	0.50	0.75	1.00
$CuFe_2O_4$, k (min^{-1})	0.226	0.286	0.071	0.037
$ZnFe_2O_4$, k (min^{-1})	0.224	0.267	0.218	0.105
$NiFe_2O_4$, k (min^{-1})	0.089	0.138	0.130	0.103
$CoFe_2O_4$, k (min^{-1})	0.076	0.078	0.054	0.050

Fig. 6 (A) Control experiments for photocatalytic degradation in the presence of $NiFe_2O_4$. The reaction conditions are: (a) MB + light, (b) MB + H_2O_2 + dark, (c) MB + H_2O_2 + light, (d) MB + ferrite + dark, (e) MB + ferrite + light, (f) MB + ferrite + H_2O_2 + dark, and (g) MB + ferrite + H_2O_2 + light. (B) Change in absorption spectra of MB with time in the presence of $NiFe_2O_4$ (0.5 g L^{-1}), pH-2.5, H_2O_2-8 mM.
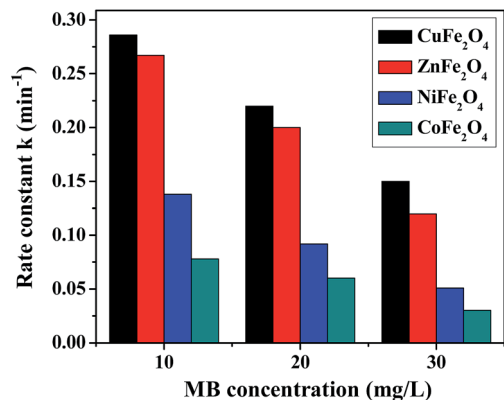
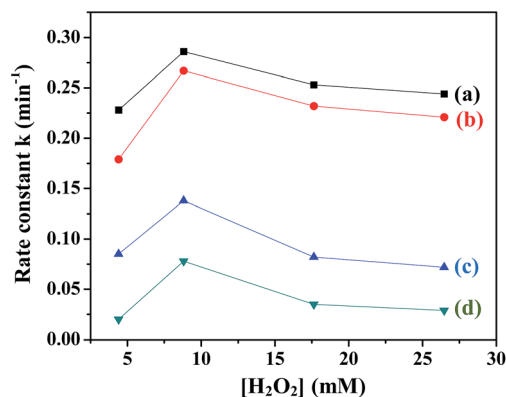**Fig. 8** Photodegradation rate of MB in the presence of the ferrites at different dye concentrations.

Fig. 9 Variation of rate constants with [H$_2$O$_2$] in the presence of (a) CuFe$_2$O$_4$, (b) ZnFe$_2$O$_4$, (c) NiFe$_2$O$_4$ and (d) CoFe$_2$O$_4$.
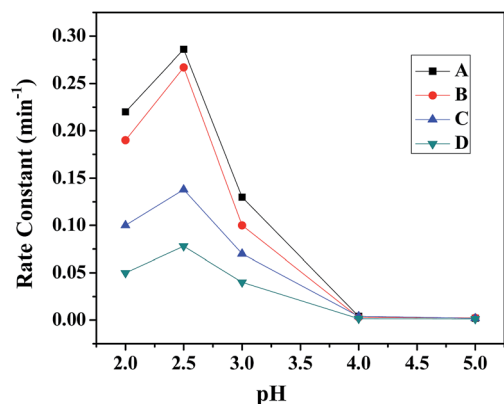
Fig. 10 Effect of pH on the rate constant in the presence of (A) CuFe$_2$O$_4$, (B) ZnFe$_2$O$_4$, (C) NiFe$_2$O$_4$ and (D) CoFe$_2$O$_4$.

the presence of light (Fig. 6(A)(g)). Hence, the presence of light, ferrite and H$_2$O$_2$ are necessary for the photo-Fenton like degradation of MB. Control experiments were performed for all the ferrites and similar results were observed.

Fig. 6(B) shows the typical absorption spectra of MB in the presence of NiFe$_2$O$_4$ nanoparticles. When H$_2$O$_2$ was added to MB solution, the peak at 246 nm was masked due to the absorption of H$_2$O$_2$ in this region. The absorption maxima gradually dropped in intensity with increasing irradiation time without the appearance of any new bands in the UV or visible region. This rapid decrease in intensity of the absorption band indicated the breakdown of the chromophore structure responsible for the color of the dye. The percentage of the dye degraded can be calculated using the following equation:[40]

$$\% \text{ degradation} = \frac{C_0 - C_t}{C_0} \times 100 \tag{3}$$

where C_0 is the initial MB concentration and C_t is the concentration at time t.

4.2 Kinetics of photocatalytic degradation

The photocatalytic degradation of MB in the presence of MFe$_2$O$_4$ (M = Co, Ni, Cu, Zn) followed pseudo first order kinetics and could be expressed according to the Langmuir–Hinshelwood (L–H) model.[39,41]

$$r = -\frac{dC}{dt} = \frac{k_r K_{LH} C}{1 + K_{LH} C} \tag{4}$$

where r (mg L^{-1} min^{-1}) is the rate of reaction, k_r (mg L^{-1} min^{-1}) is the reaction rate constant, K_{LH} (L mg^{-1}) is the adsorption rate constant, C (mg L^{-1}) is the reactant concentration and t (min) is the irradiation time. In the present reaction, the initial concentration of MB was low; therefore, the rate can be expressed as:

$$r = -\frac{dC}{dt} = \frac{k_r K C}{1 + K_{LH} C} = kC \tag{5}$$

where k (min^{-1}) is the pseudo first order rate constant and by integrating at the limit of $C = C_0$ at $t = 0$, eqn (5) can be expressed as:

$$\ln \frac{C_0}{C} = kt \tag{6}$$

The plots of ln (C_0/C) vs. t for all the ferrites are shown in Fig. 7 and the rate constants of the reaction obtained from the slopes are tabulated in Table 2.

4.3 Factors influencing photocatalytic degradation

(a) Catalyst loading. Catalyst loading is one of the important parameters in photocatalytic processes. Therefore, experiments were carried out to determine the optimum amount of catalyst dosage for the reaction. An investigation into the effect of MFe$_2$O$_4$ (M = Cu, Zn, Ni, Co) concentrations on the photodegradation of MB dye was performed by varying the amount of catalyst from 0.25 g L^{-1} to 1.00 g L^{-1} at a constant dye concentration of 10 mg L^{-1}, with 8 mM H$_2$O$_2$ at pH 2.5. All the reactions followed pseudo first order kinetics and the rate constants are tabulated in Table 2. It was interesting to note that in the initial stages the rate of the reaction increased with an increase in the dosage of catalyst; however, after a certain value

it declined. The initial elevation in the rate of reaction may be due to an increase in the total active sites on the surface of catalyst, then when the catalyst exceeded the optimum value, the rate constant dropped due to an increase in the turbidity of solution which caused a reduction in light penetration through the solution.[41,42] On the basis of the above observations all the experiments were performed with 0.5 g L^{-1} of photocatalyst.

(b) **Dye concentration.** The initial MB concentration has a significant effect on the rate of photodegradation and this was determined for all the ferrites by varying the dye concentration from 10–30 mg L^{-1} at a constant catalyst loading of 0.5 g L^{-1}, pH 2.5, with 8 mM H$_2$O$_2$. The photodegradation of MB in the presence of all the ferrites at different dye concentrations is shown in Fig. 8. The observed results reveal a decrease in the rate of degradation with an increase in the dye concentration. This could be explained by the fact that there was limited production of the hydroxyl radical (OH$^{\bullet}$) in the solution while the number of dye molecules was increasing, causing a reduction in the rate of reaction. Another reason might be explained by the Beer–Lambert law, according to which as the initial dye concentration increased, the path length of photons entering the solution decreased, resulting in a decrease in the rate.[43]

(c) **H$_2$O$_2$ concentration.** The influence of H$_2$O$_2$ concentration on the rate of degradation of MB in the presence of all the ferrites was investigated by varying the H$_2$O$_2$ concentration from 4 mM to 27 mM. Fig. 9 shows the variation in the rate constants with H$_2$O$_2$ concentration in the presence of the ferrites. It was observed that the value of rate constant initially increased with an increase in the H$_2$O$_2$ concentration up to 8

mM and then decreased. The initial increase was expected due to the reaction of H$_2$O$_2$ with ferrite to yield OH$^{\bullet}$. However, the addition of a large amount of oxidant may cause scavenging of OH$^{\bullet}$, thus not only decreasing the rate of reaction but also leading to wastage of H$_2$O$_2$ (eqn (7) and (8)).[44]

$$OH^{\bullet} + H_2O_2 \rightarrow H_2O + HOO^{\bullet} \qquad (7)$$

$$HOO^{\bullet} + OH^{\bullet} \rightarrow H_2O + O_2 \qquad (8)$$
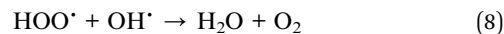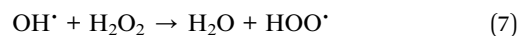
In order to achieve a high degradation rate of MB, the concentration of H$_2$O$_2$ should be optimum and was fixed at 8 mM.

(d) **Variation of pH.** The pH of the solution is one of the significant factors in the photo-Fenton like degradation of dyes and this effect was studied for all the ferrites. Fig. 10 shows the effect of pH (range 2–5) on the degradation of MB in the presence of all the ferrites through a heterogeneous photo-Fenton like process. It was seen that the removal efficiency was ~99% at pH 2.5 and an increase in the pH of the solution lead to a decrease in the removal efficiency. This outcome might be due to the formation of Fenton's reagent at lower pH to generate OH$^{\bullet}$ (hydroxyl radical), which is the main active species for the degradation of dye.[45] Therefore, the initial pH was adjusted to 2.5 for further experiments.

(e) **Effect of annealing temperature.** The photocatalytic activity of metal oxide nanoparticles is strongly influenced by particle size, morphology and surface area. Jadhav et al. reported the effect of sintering temperature on photodegradation of


Fig. 11 Effect of annealing temperature on the photocatalytic activity of the ferrites.

methyl orange using $ZnFe_2O_4$.[46] Fig. 11 displays the concentration curves of MB in the presence of all four ferrites annealed at 400 °C and 1000 °C. The results indicate that the samples annealed at 400 °C had a higher efficiency as compared to the samples annealed at 1000 °C. The decrease in photocatalytic activity of the samples annealed at 1000 °C might be attributed to the increased particle size and decreased surface area with the increase in annealing temperature. This increase in particle size was confirmed by TEM.

4.4 Mechanism of photodegradation

The possible mechanism for photodegradation of MB over MFe_2O_4 (M = Co, Ni, Cu, Zn) is outlined in Fig. 12(A). The active species for photodegradation of the dye could be produced *via* 3 pathways:

When ferrite was irradiated in the presence of visible light, an electron/hole (e^-/h^+) pair was generated on the surface (eqn (9)):

$$MFe_2O_4 + h\nu \rightarrow MFe_2O_4 \ (e_{CB}^- + h_{VB}^+) \tag{9}$$
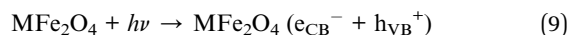
(i) The photogenerated hole h_{VB}^+ could react with water or a hydroxyl ion (H_2O or OH^-) to generate a hydroxyl radical (eqn (10) and (11)).

$$h_{VB}^+ + H_2O \rightarrow H^+ + OH^\bullet \tag{10}$$

$$h_{VB}^+ + OH^- \rightarrow OH^\bullet \tag{11}$$

(ii) The photogenerated electron e_{CB}^- could be captured by H_2O_2 to yield $OH^\bullet$, limiting the recombination of holes and electrons and thus enhancing the photocatalytic activity.

$$H_2O_2 + e_{CB}^- \rightarrow OH^- + OH^\bullet \tag{12}$$

(iii) The reaction of H_2O_2 with Fe(III) (on the surface of the ferrite) and Fe(II) generated a Fenton reagent which produced a hydroxyl radical.

$$Fe^{3+} + H_2O_2 \rightarrow Fe^{2+} + HOO^\bullet + H^+ \tag{13}$$

$$Fe^{2+} + H_2O_2 \rightarrow Fe^{3+} + OH^\bullet + OH^- \tag{14}$$
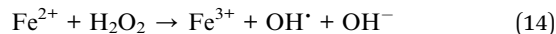
Since $OH^\bullet$ was produced by 3 pathways, an enhancement in the rate of degradation was observed. The hydroxyl radical produced by the above 3 pathways was the main active species for the degradation of MB.

4.4.1 Verification of mechanism. To evaluate the role of $^\bullet OH$ in the mechanism, the photodegradation reaction was carried out in the presence of a known $^\bullet OH$ scavenger, isopropyl alcohol (IPA). Fig. 13 shows the effect on the rate constant when the reaction was carried out in the presence and absence of the scavenger. The results indicate that the degradation rate was markedly depressed when IPA was added to the reaction mixture, suggesting, that the main active species during the reaction was $^\bullet OH$.

4.5 Comparative study of MFe_2O_4 (M = Zn, Cu, Ni and Co) for the degradation of MB

Under optimum reaction conditions ([ferrite] 0.5 g L^{-1}, [MB] 10 mg L^{-1}, pH 2.5, [H_2O_2] 8 mM), the degradation of MB was carried out using all the ferrites annealed at 400 °C. The order of reactivity evaluated from the rate constants (Table 2) is $CuFe_2O_4$ > $ZnFe_2O_4$ > $NiFe_2O_4$ > $CoFe_2O_4$.

The generation of a Fenton reagent can be tuned by substitution of transition metals such as Cu, Zn, Ni and Co in Fe_3O_4. The catalytic activity in the case of ferrites is mainly due to the metal ions in octahedral sites. The mechanism of electron transfer is given in Fig. 12(B). The cations in the octahedral site accelerate the electron transfer to regenerate Fe^{2+}, hence increasing the catalytic activity.

In the case of $CuFe_2O_4$, very high activity is observed. This may be attributed to the fact that Cu^{2+} can also produce a Fenton-like reagent, as demonstrated in following equations:[47]

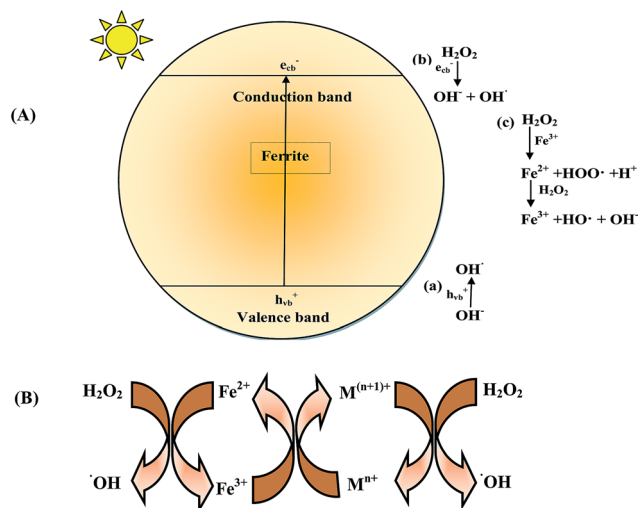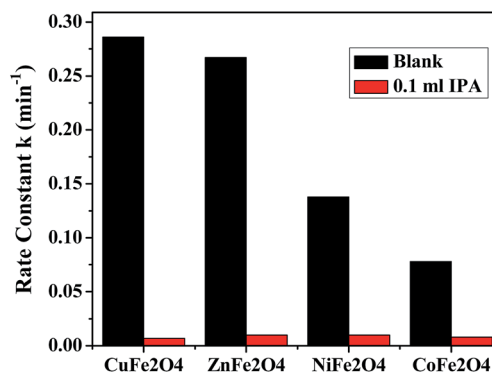$$Cu^+ + H_2O_2 \rightarrow Cu^{2+} + OH^\bullet + OH^- \tag{15}$$

Fig. 12 (A) Mechanism of generation of a hydroxyl radical (OH$^\bullet$) in the presence of a ferrite/H_2O_2/light system. (B) General mechanism of electron transfer occurring in ferrite.
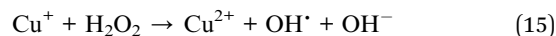

Fig. 13 Effect of addition of IPA on the degradation reactions in the presence of the ferrites.

Table 3 Comparison of results of the synthesized ferrites with photocatalysts reported in the literature for degradation of MB

S. no.	Photocatalyst	Concentration of MB	Time (min)	% degradation	Reference no.
1	Sphere like ZnO	5 mg L^{-1}	1103	97	48
2	CdS nanoparticles	4 mg L^{-1}	140	76	49
3	In_2O_3 thin films	5 mg L^{-1}	240	85	50
	ZnO thin films		240	55	
	SnO_2 thin films		240	38	
	TiO_2 thin films		240	70	
4	Reduced graphene oxide/TiO_2/ZnO	0.3 mg L^{-1}	120	92	51
5	Cu doped ZnS	10 mg L^{-1}	180	100	52

$$Cu^{2+} + H_2O_2 \rightarrow Cu^+ + HOO^{\cdot} + H^+ \qquad (16)$$

The formation of the Cu^+/Cu^{2+} redox pair causes formation of more $OH^{\cdot}$ radicals leading to the high activity of $CuFe_2O_4$.

This order can be related with the band gap of the ferrites. It is well known from literature that the lower the band gap, the higher the photocatalytic activity. This trend was followed in all the ferrites except the cobalt ferrite. The band gap of the cobalt ferrite was lowest but its photocatalytic activity was the least. This might be due to the recombination of the photogenerated e^-/h^+ pair. It was also observed that the activity of ferrites does not depend on the surface area calculated from BET. The catalytic activity of the ferrites could also be correlated with the magnetization values. Based on the charge and size, the metal ions possess an inherent ability to occupy either the tetrahedral or the octahedral site of the ferrite sub lattice. The catalytic activity of the ferrites is also due to metal ions in the octahedral sites. The high activity of $CuFe_2O_4$ can be correlated to the tendency of Cu^{2+} to occupy the octahedral site,[48] which enables easy electron exchange between the variable oxidation states of Cu.

4.6 Contrast of synthesized photocatalysts with literature precedents

A detailed literature review illustrated the use of different photocatalysts for the degradation of MB.[49–53] Hence, comparison of the

Fig. 14 Reusability of the ferrites for 4 successive cycles under similar conditions.

photodegradation efficiency of various photocatalysts with the present system was done and is shown in Table 3. Entries in Table 3 clearly demonstrate the superiority of the synthesized spinel ferrites in terms of photocatalytic performance. In addition, all the synthesized materials possess the advantages of being stable, magnetically recoverable and recyclable after the reaction without any significant loss in activity.

4.7 Recyclability

The stability and recyclability of photocatalysts is of prime importance for their potential application in long-term processes to decompose organic pollutants that are present in waste water. Ferrites possess heterogeneous photo-Fenton like activity and excellent magnetic properties, hence they can be easily separated from the reaction mixture using an external magnet. After completion of the reaction, the catalyst was magnetically separated, washed 5 times with distilled water followed by drying in an oven at 100 °C. The recovered catalyst was again redispersed in fresh MB solution for the next cycle. None of the ferrite nanoparticles exhibited any significant loss of activity even after four cycles, thus demonstrating the high stability of the synthesized photocatalyst and hence confirming their promise for application in waste water treatment. The typical degradation percentage of MB in the presence of all the ferrites for 4 successive cycles is shown in Fig. 14.

5. Conclusion

To conclude, visible light active nanospinels MFe_2O_4 (M = Ni, Cu, Zn, Co) were successfully fabricated via a sol–gel method for the photo-Fenton like degradation of MB. The formulated ferrites in the nano range were well characterized by various techniques. The present study revealed the role of the cation in the degradation process as the most effective catalyst out of the four ferrites was $CuFe_2O_4$ (~99% degradation in 15 min) followed by $ZnFe_2O_4$, $NiFe_2O_4$ and $CoFe_2O_4$. The optimum reaction conditions were determined and an investigation of kinetics revealed that the reactions are pseudo first order. The prepared materials possessed excellent magnetic properties thus leading to their easy separation from aqueous solution by an external magnet without an additional filtration step. Furthermore, the results indicated that the catalyst could be reused up to four times without any significant loss of activity, hence indicating its potential for application for the photo-Fenton like degradation of organic pollutants from wastewater.

Acknowledgements

References

1 D. Wang and D. Astruc, *Chem. Rev.*, 2014, **114**, 6949–6985.

2 L. M. Rossi, N. J. S. Costa, F. P. Silva and R. Wojcieszak, *Green Chem.*, 2014, **16**, 2906–2933.

3 T. Cheng, D. Zhang, H. Li and G. Liu, *Green Chem.*, 2014, **16**, 3401–3427.

4 K. Lazar, T. Mathew, Z. Koppany, J. Megyeri, V. Samuel, S. P. Mirajkar, B. S. Rao and L. Guczi, *Phys. Chem. Chem. Phys.*, 2002, **4**, 3530–3536.

5 R. Hudson, Y. Feng, R. S. Varma and A. Moores, *Green Chem.*, 2014, **16**, 4493–4505.

6 C. S. Hwang and N. C. Wang, *Mater. Chem. Phys.*, 2004, **88**, 258–263.

7 A. S. Singh, S. S. Shendage and J. M. Nagarkar, *Tetrahedron Lett.*, 2013, **54**, 6319–6323.

8 F. Papa, L. Patron, O. Carp, C. Paraschiv and B. Ioan, *J. Mol. Catal. A: Chem.*, 2009, **299**, 93–97.

9 J. Tsagaroyannis, K. J. Haralambous, Z. Loizos, G. Petroutsos and N. Spyrellis, *Mater. Lett.*, 1996, **28**, 393–400.

10 Y. J. Tu, C. F. You, C. K. Chang, S. L. Wang and T. S. Chan, *Chem. Eng. J.*, 2013, **225**, 433–439.

11 E. Casbeer, V. K. Sharma and X. Z. Li, *Sep. Purif. Technol.*, 2012, **87**, 1–14.

12 M. A. Gibson and J. W. Hightower, *J. Catal.*, 1976, **41**, 420–430.

13 M. I. Zaki, W. Ramadan, A. Katrib and A. I. M. Rabee, *Appl. Surf. Sci.*, 2014, **317**, 929–934.

14 X. Li, Y. Hou, Q. Zhao, W. Teng, X. Hua and G. Chen, *Chemosphere*, 2011, **82**, 581–586.

15 X. Li, Y. Hou, Q. Zhao and L. Wang, *J. Colloid Interface Sci.*, 2011, **358**, 102–108.

16 Y. Sun, W. Wang, L. Zhang, S. Sun and E. Gao, *Mater. Lett.*, 2013, **98**, 124–127.

17 N. M. Mahmoodi, *Mater. Res. Bull.*, 2013, **48**, 4255–4360.

18 M. Su, C. He, V. K. Sharma, M. A. Asi, D. Xia, X. Z. Li, H. Deng and Y. Xiong, *J. Hazard. Mater.*, 2012, **211–212**, 95–103.

19 X. Feng, G. Y. Mao, F. X. Bu, X. L. Cheng, D. M. Jiang and J. S. Jiang, *J. Magn. Magn. Mater.*, 2013, **343**, 126–132.

20 W. Wang, N. Li, Y. Chi, Y. Li, W. Yan, X. Li and C. Shao, *Ceram. Int.*, 2013, **39**, 3511–3518.

21 J. An, L. Zhu, Y. Zhang and H. Tang, *J. Environ. Sci.*, 2013, **25**(6), 1213–1225.

22 W. Luo, L. Zhu, N. Wang, H. Tang, M. Cao and Y. She, *Environ. Sci. Technol.*, 2010, **44**, 1786–1791.

23 M. Sajjia, M. Oubaha, M. Hasanuzzaman and A. G. Olabi, *Ceram. Int.*, 2014, **40**, 1147–1153.

24 G. B. Teh, Y. C. Wong and R. D. Tilley, *J. Magn. Magn. Mater.*, 2011, **323**, 2318–2322.

25 S. Sutradhar, S. Pati, S. Acharya, S. Das, D. Das and P. K. Chakrabarti, *J. Magn. Magn. Mater.*, 2012, **324**, 1317–1325.

26 P. Sivakumar, R. Ramesh, A. Ramanand, S. Ponnusamy and C. Muthamizhchelvan, *Appl. Surf. Sci.*, 2012, **258**, 6648–6652.

27 T. Slatineanu, A. R. Iordan, M. N. Palamaru, O. F. Caltun, V. Gafton and L. Leontie, *Mater. Res. Bull.*, 2011, **46**, 1455–1460.

28 M. A. Gabal, R. S. Al-luhaibi and Y. M. Al Angari, *J. Hazard. Mater.*, 2013, **246–247**, 227–233.

29 M. G. Naseri, E. B. Saion, H. A. Ahangar, M. Hashim and A. H. Shaari, *J. Magn. Magn. Mater.*, 2011, **323**, 1745–1749.

30 S. Kimura, T. Mashino, T. Hirokia, D. Shigeoka, N. Sakai, L. Zhu and Y. Ichiyanagi, *Thermochim. Acta*, 2012, **532**, 119–122.

31 P. Pascuta, A. Vladescu, G. Borodi, E. Culea and R. Tetean, *Ceram. Int.*, 2011, **37**, 3343–3349.

32 A. Hassadee, T. Jutarosaga and W. Onreabroy, *Procedia Eng.*, 2012, **32**, 597–602.

33 A. I. Nandapure, S. B. Kondawar, P. S. Sawadh and B. I. Nandapure, *Phys B Condens Matter*, 2012, **407**, 1104–1107.

34 M. Ajmal and A. Maqsood, *J. Alloys Compd.*, 2008, **460**, 54–59.

35 P. Guo, G. Zhang, J. Yu, H. Li and X. S. Zhao, *Colloids Surf., A*, 2012, **395**, 168–174.

36 S. A. Saafan, S. T. Assar, B. M. Moharram and M. K. El Nimr, *J. Magn. Magn. Mater.*, 2010, **322**, 628–632.

37 A. K. Ladavos, A. P. Katsoulidis, A. Iosifidis, K. S. Triantafyllidis, T. J. Pinnavaia and P. J. Pomonis, *Microporous Mesoporous Mater.*, 2012, **151**, 126–133.

38 M. A. Rauf, M. A. Meetani, A. Khaleel and A. Ahmed, *Chem. Eng. J.*, 2010, **157**, 373–378.

39 T. Soltani and M. H. Entezari, *J. Mol. Catal. A: Chem.*, 2013, **377**, 197–203.

40 T. Xie, L. Xu, C. Liu and Y. Wang, *Appl. Surf. Sci.*, 2013, **273**, 684–691.

41 T. Soltani and M. H. Entezari, *Ultrason. Sonochem.*, 2013, **20**, 1245–1253.

42 K. N. Harish, H. S. B. Naik, P. N. P. Kumar and R. Viswanath, *ACS Sustainable Chem. Eng.*, 2013, **52**, 8174–8181.

43 M. H. Habibi, N. Talebian and J. H. Choi, *Dyes Pigm.*, 2007, **73**, 103–110.

44 F. D. Mai, C. C. Chena, J. L. Chen and S. C. Liu, *J. Chromatogr. A*, 2008, **1189**, 355–365.

45 B. Sahoo, S. K. Sahu, S. Nayak, D. Dhara and P. Pramanik, *Catal. Sci. Technol.*, 2012, **2**, 1367–1374.

46 S. D. Jadhav, P. P. Hankare, R. P. Patil and R. Sasikala, *Mater. Lett.*, 2011, **65**, 371–373.

47 X. Zhang, Y. Ding, H. Tang, X. Han, L. Zhu and N. Wang, *Chem. Eng. J.*, 2014, **236**, 251–262.

48 S. Bhukal, Shivali and S. Singhal, *Mater. Sci. Semicond. Process.*, 2014, **26**, 467–476.

49 M. BoraAkinn and M. Oner, *Ceram. Int.*, 2013, **39**, 9759–9762.

50 X. Li, C. Hu, X. Wang and Y. Xi, *Appl. Surf. Sci.*, 2012, **258**, 4370–4376.

51 N. Talebian and M. R. Nilforoushan, *Thin Solid Films*, 2010, **518**, 2210–2215.

52 N. Raghavan, S. Thangavel and G. Venugopal, *Mater. Sci. Semicond. Process.*, 2015, **30**, 321–329.

53 R. Chauhan, A. Kumar and R. P. Chaudhary, *J. Lumin.*, 2014, **145**, 6–12.